CEAS-GNC-2024-060

EuroGNC Navigation Guidance Control CEAS Bristol, UK June 11th-13th 2024
University of BRISTOL ROYAL AERONAUTICAL SOCIETY AIAA

Worst-case Uncertainty Methods in the Precise Pointing Control of Flexible Spacecraft

János Bezsilla Developer, Institute for Computer Science and Control, Systems and Control Lab, 1111, Budapest, Hungary. bjanos96@gmail.com

Bálint Patartics Research Fellow, Institute for Computer Science and Control, Systems and Control Lab, 1111, Budapest, Hungary. patartics@sztaki.hu

Jian Guo Associate Professor, Delft University of Technology, Space Systems Engineering, 2629HS, Delft, The Netherlands. j.guo@tudelft.nl

Bálint Vanek Deputy Director, Institute for Computer Science and Control, Systems and Control Lab, 1111, Budapest, Hungary. vanek@sztaki.hu

Béla Takarics Senior Research Fellow, Institute for Computer Science and Control, Systems and Control Lab, 1111, Budapest, Hungary. takarics@sztaki.hu

ABSTRACT

Nowadays, many space missions require highly accurate pointing for Earth observation or cosmic vision purposes. However, the vibration environment from a spacecraft's structure and reaction wheels can cause disturbances in its line-of-sight stability and severely impact image quality. Additionally, these effects are not known precisely due to limitations in ground testing, and this uncertainty leads to significant challenges in control. This paper tackles these problems by creating a control design and verification framework. Modern scientific literature explores three solutions: high-fidelity nonlinear modelling, advanced control design methods, and optimized verification campaigns. Respectively, they provide a reliable testing environment, directly handle structural dynamics, and guarantee system stability. While the three approaches are usually studied separately, we propose a novel combination using a payload isolation platform. A robust H_∞-based cascade control loop is designed for a Sentinel-like spacecraft and analyzed to maximize pointing indicators in a realistic mission scenario and then validated using a worst-case uncertainty construction method via multi-frequency gain maximization. The synergy of the framework offers a robust solution for precise pointing in flexible spacecraft and enables further mass reductions in the future of space exploration.

Keywords: flexible spacecraft; high-fidelity modeling; precise pointing; robust control; verification and validation

Nomenclature

ϕ, θ, ψ	=	Euler angles (roll, pitch, yaw)
$\boldsymbol{\tau}_A^F$	=	Torque acting in point A (or COG) and frame F
ω_{BA}^F	=	Angular velocity of B compared to A in frame F
$\mathbf{f}_A^F$	=	Force acting in point A (or COG) and frame F

$\mathbf{G}(s)$ = System
$\mathbf{J}$ = Inertia matrix
$\mathbf{K}(s)$ = Controller
m = Mass
$\mathbf{q}_{BA}$ = Rotation quaternion from frame A to B
$\mathbf{r}_{BA}^{F}$ = Position vector from point A to B in frame F
$\mathbf{R}_{BA}$ = Rotation matrix from frame A to B
s = Laplace variable
$\mathbf{v}_{BA}^{F}$ = Velocity of B compared to A in frame F^{-1}
$\mathbf{W}(s)$ = Weighing function

1 Introduction

Nowadays, there are many ongoing and proposed missions involving spacecraft where extremely accurate pointing is required, either for cosmic vision or Earth observation purposes. These applications usually require rigid vehicles, otherwise, a number of disturbing effects would severely impact image quality and line-of-sight stability, such as flexible appendages and internal microvibration sources [1]. Flexible appendages tend to be prevalent in complex missions, as payload mass restrictions can often only be met with low-stiffness structures. Their vibration characteristics are imprecisely known because the gravity environment on Earth does not allow for rigorous testing. This uncertainty of frequency and damping of the flexible modes and potential coupling between axes leads to major challenges in attitude determination and control system (ADCS) design [2]. Additionally, manufacturing imperfections in reaction wheels generate residual harmonic microvibrations which can be amplified on interaction with the structure of the spacecraft, perturbing the onboard instrumentation's line-of-sight stability or even leading to structural failure. As a result, accurately predicting spacecraft microvibrations due to onboard internal disturbance sources is a formidable multi-disciplinary engineering challenge [3]. The proposed work aims to tackle the control problem of stabilizing the flexible system while also aiming to increase pointing performance.

In the scientific literature on flexible spacecraft, there are many notable proposals to solve this challenge, such as sliding mode attitude tracking control [4], integrated spacecraft design with structured H_∞ control design [5], or even the predictive control of flexible spacecraft [6]. As one of the first high-precision flexible spacecraft in orbit, JAXA's Advanced Land Observing Satellite proved to be an important source of hardware data and engineering experience, especially when it comes to assessing state-of-the-art sensor and actuator characteristics [7]. On the topic of vibration isolation and suppression, an investigation of space applications of active-passive platforms yielded promising articles by Preda that combine robust microvibration mitigation with pointing performance analysis [8], as well as the use of Stewart Platform in cascade control structures [9]. It has been noted that literature on the verification of controllers for flexible spacecraft is rather lacking, with very few published articles in the field. This is the gap that this project is trying to fill, by building on the body of research accumulated over the years on the topics that have previously been discussed. Important publications include the work of Wang on verification [10] and robustness analysis [11], as well as the work of Gasbarri [2] on worst-case analysis.

Based on these findings, it was determined that the best approach to achieve higher pointing precision in flexible spacecraft is the analysis and validation of advanced controllers in a nonlinear simulation environment. The main contribution of this paper is the space application of a novel verification method using multi-frequency worst-case analysis [12], building on the previous publication of the research group on the parameter uncertainty analysis of linear controllers for the pointing problem [13], and proposing a cascade control loop using robust methods. Section 2 covers the modelling aspects of a flexible spacecraft in orbit, taking into account flexible appendages, mechanical spinning devices, and

the coupling between the satellite body and the payload platform. Section 3 presents a full attitude determination and control system (ADCS) chain via the design of an H_∞-based controller that satisfies predefined pointing performance requirements and offers acceptable disturbance rejection characteristics. Finally, section 4 showcases the V&V framework that makes use of the developed high-fidelity nonlinear simulation environment.

2 Modelling the Spacecraft

To describe and analyze the dynamics of the nonlinear system, a realistic mathematical model was built in Simulink. The resulting system achieves high fidelity in modelling the dynamics of an Earth-observing spacecraft while still retaining a high simulation speed due to the efforts made to increase efficiency. To numerically solve the differential equations, the Bogacki-Shampine method is used with a fixed time step of 1 ms. Throughout the paper, Sentinel-2B, a European Earth observation satellite is used as a reference spacecraft for both orbit modelling and system characteristics. This features a spacecraft bus with a similar size and mass to the original, a rotating solar panel, and a variable-mass propellant tank. This reference spacecraft (as well as Sentinel-2B) occupies a Sun-synchronous orbit, which is highly inclined and circular at 790 km altitude. For accurate orbit modelling, the orbital parameters are frequently updated from the spacecraft's two-line orbital elements [13].

2.1 Equations of Motion

This paper uses five reference frames to describe the translational and rotational motion of the body: Earth-Centered Inertial (ECI or I), Earth-Centered Earth-Fixed (ECEF or F), Local Vertical Local Horizontal (LVLH or L), Body (B), and Payload (P). Four state vectors are defined in the derivation of the equations of motion: the ECEF-frame position vector ($\mathbf{r}_{BF}^F$), the ECEF-frame velocity vector ($\mathbf{v}_{BF}^F$) of the spacecraft, the ECEF-to-Body rotation quaternion ($\mathbf{q}_{BF}$), and the Body-frame angular velocity of the spacecraft ($\boldsymbol{\omega}_{BI}^B$). $\boldsymbol{\omega}_\oplus^F$ is the rotation rate of Earth [13].

$$\begin{gathered}\dot{\mathbf{r}}_{BF}^F = \mathbf{v}_{BF}^F \qquad \dot{\mathbf{v}}_{BF}^F = \mathbf{R}_{FB}\frac{\mathbf{f}^B}{m} - 2\boldsymbol{\omega}_\oplus^F \times \mathbf{v}_{BF}^F - \boldsymbol{\omega}_\oplus^F \times \left(\boldsymbol{\omega}_\oplus^F \times \mathbf{r}_{BF}^F\right) \\ \dot{\boldsymbol{\omega}}_{BI}^B = \mathbf{J}^{-1}\left[\boldsymbol{\tau}^B - \boldsymbol{\omega}_{BI}^B \times \left(\mathbf{h}_{rw}^B + \mathbf{J}\boldsymbol{\omega}_{BI}^B\right)\right] \qquad \dot{\mathbf{q}}_{BF} = \frac{1}{2}\mathbf{q}_{BF} \circ \mathring{\boldsymbol{\omega}}_{BF}^B \qquad \mathring{\boldsymbol{\omega}}_{BF}^B = \begin{bmatrix} 0 \\ \boldsymbol{\omega}_{BI}^B - \mathbf{R}_{BF}\boldsymbol{\omega}_\oplus^F \end{bmatrix}\end{gathered} \tag{1}$$

Additionally, the orientation of the spacecraft is defined to be the quaternion between the Body and the local frames. This quaternion also serves as the basis for the Local-to-Body rotation matrix, as well as the definition of Euler angles with an XYZ rotation order, which reduces the Yaw angle to a rotation around the optical axis to simplify the pointing control problem.

$$\mathbf{q}_{BL} = \mathbf{q}_{BF}\mathbf{q}_{LF}^{-1} \longrightarrow \mathbf{R}_{BL} \longrightarrow \phi, \theta, \psi \tag{2}$$

There are a number of environmental factors that have undesirable effects on the dynamics of the spacecraft by changing its overall momentum (linear or angular). This paper will mainly focus on external torques, which can vary greatly in magnitude. In order to preserve computational efficiency, the main goal is not to model them as numerically accurately as possible but rather to build optimized representations of them that match their real-world frequency and magnitude characteristics. At the altitude of the spacecraft, the main disturbing effects are gravity gradient, magnetism, and drag [13].

2.2 Structural Dynamics

A major source of disturbance to the spacecraft comes from its structural dynamics, as the solar panel attached to the side of the satellite acts as a flexible appendage. In this project, the panel is considered to be a flexible beam element with a rigid single-point connection to the spacecraft. This description of the flexible body results in a linear state-space model, following the derivation of pure flexion dynamics from Chebbi et al [14]. Using the approach, a linear model was derived for the x-y bending modes of the beam element representing the solar panel, and the final model was verified against the `Satellite Dynamics Toolbox` of Alazard et al [15–17].

The linear model is integrated into the nonlinear simulation environment by dropping the purely rigid components from the structural model as they are already represented in the spacecraft equations of motion. The frequency response of the resulting flexible system resembles a high-pass filter with a cutoff frequency of roughly 17 rad/s. This is ideal for control purposes as the frequency is well within the bounds of available spacecraft actuators. There are three more resonant frequencies for the appendage (at roughly 109, 311, and 1383 rad/s). The largest frequency bending mode is uncontrollable, but fortunately has a low magnitude and can still be simulated with the current time step, so its effect on control performance can still be evaluated [13].

2.3 Reaction Wheels

On most modern spacecraft, the primary instruments for attitude control actuation are reaction wheels. They are essentially torque motors with a high inertia rotor which can spin in either direction and can provide one axis of control. In the model, we are using one reaction wheel for each of the spacecraft's principal axes, as well as an additional fourth wheel for redundancy (NASA Standard configuration) [13].

Since the microvibration behaviour of reaction wheels has a much higher frequency than orbital or even attitude dynamics, modelling them to high fidelity would be severely detrimental to simulation speed. However, some empirical models are able to approximate these high-frequency microvibrations with a harmonic series expansion of reaction wheel dynamics [18, 19]. To account for time delays in the state estimation and the control process (assumed 0.01 s) a 5th order Padé approximant is included in the control-oriented model with a safety factor of 10 on the duration [20].

2.4 Active-Passive Payload Isolation Platform

A Stewart-Gough platform is a parallel manipulator device with linear actuators and universal joints that allow for the 6-DOF control of the payload plate. Their use in space applications is supported by a large research interest due to their inherent capability to not only provide articulation between different subsystems but also isolate microvibrations. This has the added benefit of merging two functionalities in the same mechanical system, decreasing both the complexity and the mass of the vehicle. The platform should be supported by at least 6 struts (a hexapod platform), where the configuration of the struts also influences the degree of cross-coupling in the device, which should be taken into consideration during the design process. The mathematical model of the isolation platform is largely inspired by the work of Hanieh and Preumont. Their work also involved the construction of a hardware demonstrator, whose frequency-domain characteristics should be matched as closely as possible. The goal is to build an idealized model of the hexapod device with struts capable of active-passive isolation. First off, the hexapod should follow a cubical structure with all struts being orthogonal to each other in the neutral position. This reduces the effects of cross-coupling between them to the smallest degree possible [21, 22].

The equations of motion for the payload plate are expressed in terms of relative dynamics, considering the rotating frame of the spacecraft Body and the arising Coriolis, Euler, and centrifugal forces. Rotational dynamics are also expressed in the body frame, $\mathbf{J}_I$ is the mass moment of inertia matrix of the payload plate, approximated as a flat equilateral triangle. Calculating the forces $\mathbf{f}_P^B$ and torques $\boldsymbol{\tau}_P^B$ acting on the

payload plate is done by the summation of actuator forces $\mathbf{f}_a$ with the stiffness and damping reactions of the struts. Then, the resulting forces and torques can be reduced to the payload frame through the transform matrix $\mathbf{J}_{BP}$ and Jacobian matrix $\mathbf{J}_P$ that arise from the inverse kinematics solution for hexapod robots. Despite the complexity of the dynamical equations, the kinematics are relatively simple with similar formulas used in the EOM of the spacecraft body as well [9, 21].

$$\begin{aligned} \ddot{\mathbf{x}}_P = \begin{bmatrix} \dot{\mathbf{v}}^B_{PB} \\ \dot{\boldsymbol{\omega}}^B_{PB} \end{bmatrix} &= \begin{bmatrix} \frac{1}{m_I}\mathbf{f}^B_P + \mathbf{g}^B - \dot{\mathbf{v}}^B_{BF} - 2\boldsymbol{\omega}^B_{BI} \times \mathbf{v}^B_{PB} - \dot{\boldsymbol{\omega}}^B_{BI} \times \mathbf{r}^B_{PB} - \boldsymbol{\omega}^B_{BI} \times \left(\boldsymbol{\omega}^B_{BI} \times \mathbf{r}^B_{PB}\right) \\ \mathbf{J}_I^{-1}\left(\boldsymbol{\tau}^B_P - \boldsymbol{\omega}^B_{PB} \times \mathbf{J}_I \boldsymbol{\omega}^B_{PB}\right) \end{bmatrix} \\ \dot{\mathbf{x}}_P = \begin{bmatrix} \dot{\mathbf{r}}^B_{PB} \\ \dot{\mathbf{q}}_{PB} \end{bmatrix} = \begin{bmatrix} \mathbf{v}^B_{PB} \\ \frac{1}{2}\mathbf{q}_{PB} \circ \mathring{\boldsymbol{\omega}}^B_{PB} \end{bmatrix} \qquad \begin{bmatrix} \mathbf{f} \\ \boldsymbol{\tau} \end{bmatrix}^B_P &= \mathbf{J}_{BP}\mathbf{J}_P\left[\mathbf{f}_a - c_I \delta \boldsymbol{\ell}_i - k_I\left(\boldsymbol{\ell}_i - \ell_0\right)\right] \end{aligned} \tag{3}$$

The linear actuators of the struts are saturated at ±0.05 N and have a 0.01-sec delay which is reduced in the control-oriented linearized model with a 5-th order Padé approximant. The actuators themselves are driven by electric motors with a cutoff frequency of 100 rad/s that form a 6x6 diagonal matrix to represent all struts, and body-frame forces and torques are converted to strut forces with the use of a decoupling matrix based on the force Jacobian and the force transform matrices.

$$\mathbf{G}^I_{Act}(s) = \mathbf{G}_{Strut}(s)\mathbf{D}(s)\mathbf{G}^I_{Pade}(s) \qquad \mathbf{D}_I = \left(\mathbf{J}_{BP}\mathbf{J}_P\right)^{-1} \tag{4}$$

3 Designing the Control Loop

Consider that the inputs to the spacecraft are body-frame forces and torques in all three directions, and the outputs are the accelerations and the angular accelerations of the spacecraft body along the same axes. In the simplest, rigid case for a spacecraft of mass m and moment of inertia $\mathbf{J}$ at rest in inertial space. Then, this model can be combined with the derived linear model for the structural dynamics ($\mathbf{G}_{flex}(s)$) to serve as a basis for the control-oriented model. Then, the model is reduced to only the rotational modes, and the linearized reaction wheel torques with transient behaviour related to motor dynamics ($\mathbf{G}_{RWA}(s)$), but free of vibrations and friction.

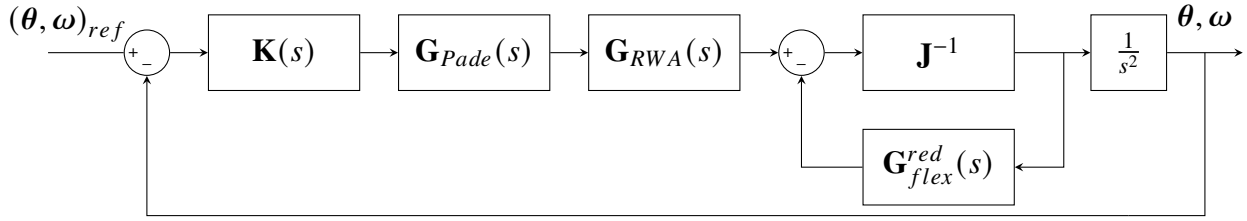

Fig. 1 Linearized system model with time delay and actuator dynamics

For the isolator loop, the final model is an expansion of $\mathbf{G}^I_F(s)$ with actuator dynamics and time delay characteristics, as presented in fig. 2. It allows the design of a collocated controller by defining the outputs as the position and orientation of the payload plate while system inputs are the overall forces and torques acting on the payload plate instead of individual strut forces.

3.1 Guidance and Navigation

To estimate the states, four states are measured and then mixed with normally distributed random noise. ECEF position is measured with GPS, Body-frame velocity with integrated accelerometer, body-frame angular velocity with a drifting gyro, and Euler angles with a star tracker. With these sensor measurements, we estimate all other states of the system by plugging them into the equations of motion.

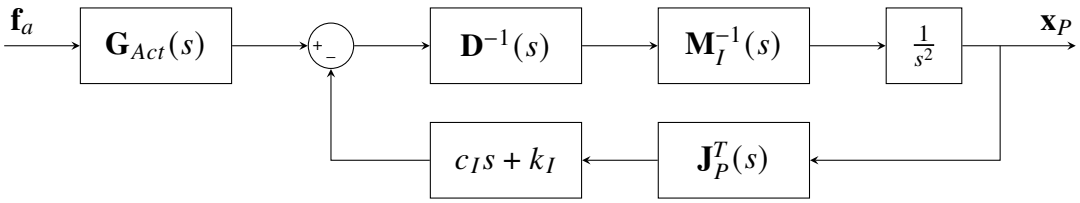

Fig. 2 Linearized isolator plant model for control design

To handle sensor drift, the integrators driven by the gyro and the accelerometer are periodically reset with lower frequency measurements from the GPS and star tracker. The isolator loop includes a virtual sensor that attempts to recreate the precision characteristics of an optical sensor that returns position and attitude measurements for the payload plate. Then, we implemented a quaternion-based algorithm for smooth trajectory generation, which relates the current line-of-sight vector of the spacecraft $\mathbf{r}_{BF}^F$ to the desired target vector $\mathbf{r}_{TF}^F$ through a single rotation. The angular velocity reference is calculated using the inverted kinematic model of the spacecraft and numeric differentiation [13].

$$\mathbf{r}_{TB}^L = \mathbf{R}_{LF}\left(\mathbf{r}_{TF}^F - \mathbf{r}_{BF}^F\right) \qquad \mathbf{i}_3 = [0 \quad 0 \quad 1]^T \qquad \mathbf{q}_{BL} \sim \left[1 + \mathbf{i}_3 \cdot \hat{\mathbf{r}}_{TB}^L \qquad \mathbf{i}_3 \times \hat{\mathbf{r}}_{TB}^L\right] \tag{5}$$

3.2 Outer Loop Design

Generally speaking, in closed-loop control design there is a trade-off between performance and robustness. The closer a controller gets to zero in reducing errors in the loop, the more sensitive it becomes to disturbances, noise, delay, and uncertainty. In recent years, there has been an increase in robust control publications for flexible spacecraft across Europe, a technique that offers to find a balance in this trade-off and increase reliability for future missions [5, 23].

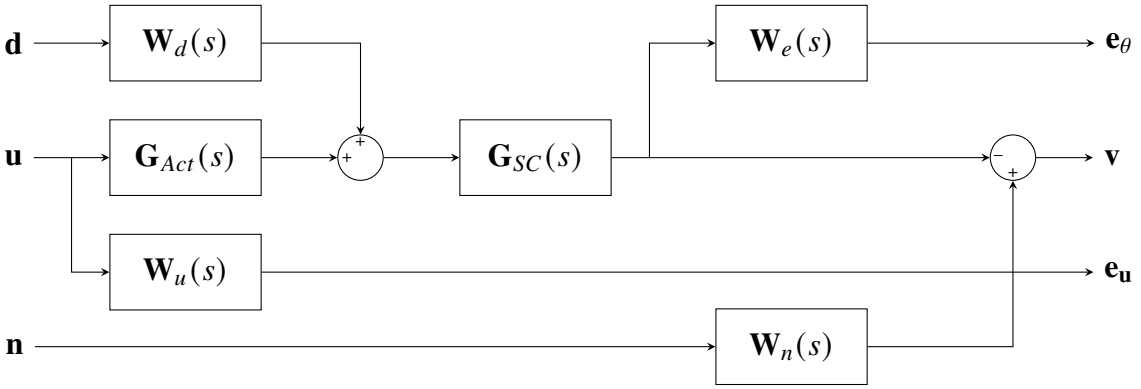

Fig. 3 Augmented plant for robust control design

In robust control, one of the most important applied methods is H_∞-based loop shaping, where the main design goal is the minimization of the H_∞ norm of the system in order to attenuate the effect of disturbances on its performance. This norm also provides a measure of system robustness as γ. In the design of the controller, various weights are added to the input and output signals of the plant model. The result is called an augmented plant (fig. 3) and is the major component of the loop-shaping process. These weights are used to prescribe desired characteristics in noise suppression, disturbance rejection, control effort, and control performance (fig. 4). During the tuning process, performance is iteratively evaluated by the step response and frequency-domain characteristics of the linearized closed-loop, as well as the pointing performance in the high-fidelity nonlinear environment for a simple scenario. The main goal is to decrease the pointing error below 2 arcsec in roll and pitch, and to find the solution that provides the most pointing stability within that range.

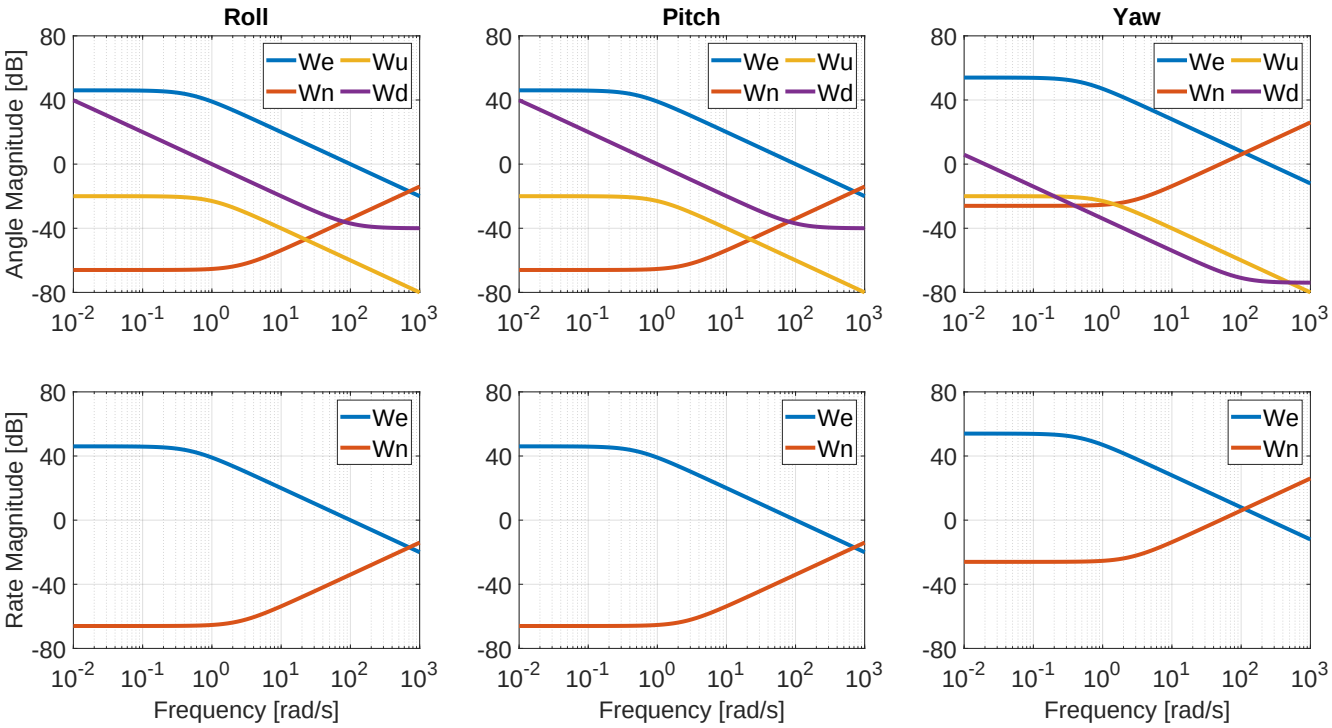

Fig. 4 Weights used in the design of H_∞-based controller

The closed-loop system that `hinfsyn` produced has a γ of 50. Since there is no explicit modelling uncertainty in the design process, γ does not give upper bounds for the Delta block, merely for the transfer from the disturbance inputs to the performance outputs. Since this transfer is scalable, a high γ can also be worked around by further scaling of the tuning weights. More concerning is the number of controller states (51). To reduce numerical complexity and improve computational performance, this must be drastically cut back. It was found that control performance is not decreased if 32 states with the lowest Hankel singular values are eliminated from the controller block. The final, 19-state H_∞-based controller can then be tested in a closed-loop to evaluate time-domain performance.

3.3 Inner Loop Design

The inner loop is chosen to be driven by an H_∞-based robust controller, however, there is an important change from the robust control design presented in the previous section. For the isolator loop, the controller is tuned to mimic a reference system in its closed-loop behaviour. This reference system is also an integral part of the augmented plant (fig. 5) with its own filters.

$$\mathbf{G}^I_{ref,diag}(s) = \frac{100}{s^2 + 20s + 100} \qquad \mathbf{G}^I_{ref,5}(s) = \frac{100}{s^2 + 4s + 100} \tag{6}$$

The rest of the filters are various low-pass and high-pass filters, as well as zero gains for off-diagonal elements (fig. 6). Similarly to the previous design, the filter parameters were tuned using a combination of intuitive initial values selected based on desired system performance and iterative tuning based on the achieved disturbance rejection and reference tracking characteristics. There were two main goals in the tuning process. First, to diminish the cross-coupling effects from X-displacement to Pitch and Y-displacement to Roll. Second, to bring the cutoff frequency of the pointing loop beyond 17 rad/s in order to actively control at least the first flexible mode of the system and achieve at least -40 dB/decade of attenuation for higher frequencies. The control synthesis algorithms concluded with a final γ of 1.0058, and the final controller had 81 states, which was reduced to the 18 largest ones in terms of Hankel singular value.

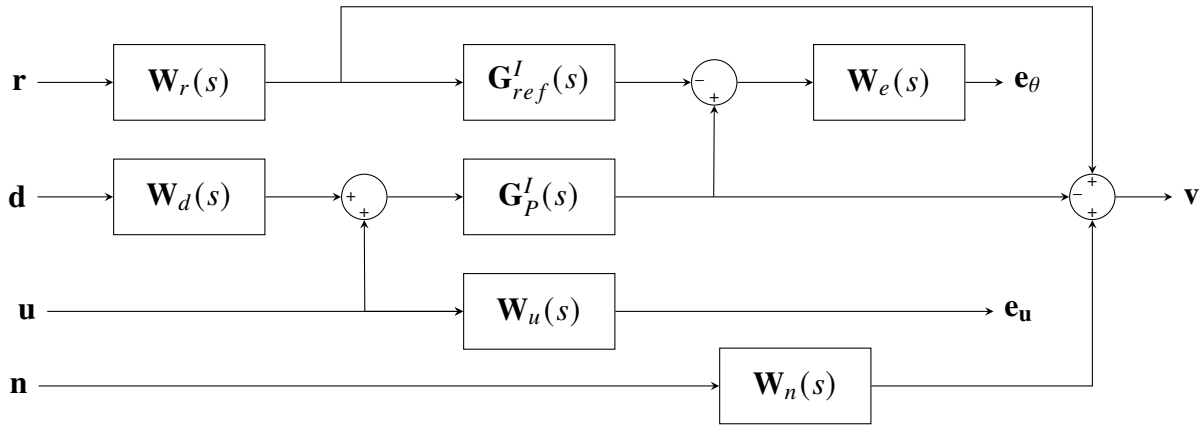

Fig. 5 Augmented plant for isolator control loop design

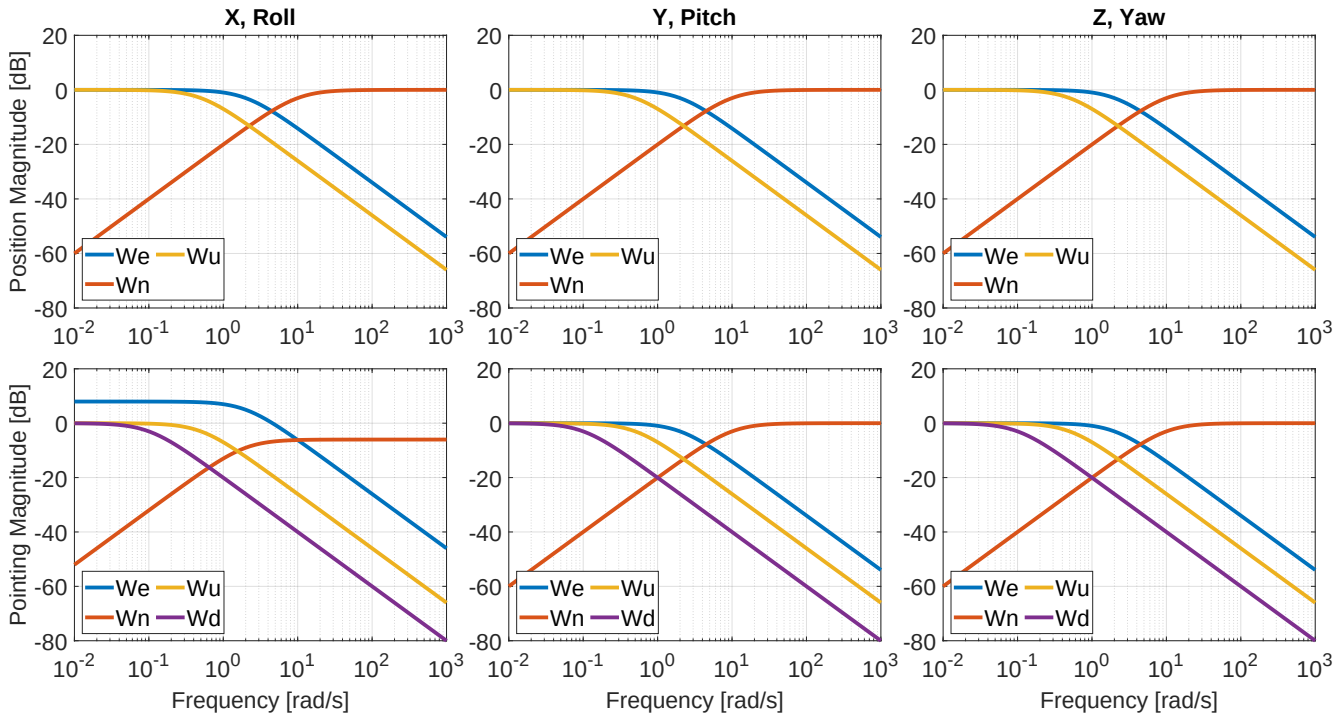

Fig. 6 Tuning weights of isolator control loop

4 Verification & Validation

Since the current robust control method only deals with uncertainty in an implicit manner, there needs to be a way to ensure the robustness of closed-loop control to known uncertain behaviours. One way of verification and validation is to use μ-analysis techniques, which rely on advanced approaches to LFT modelling (linear fractional transformation) and a significant effort in model reduction. However, even with reduction, these methods generate high-order models, which severely complicate the process of verification. As a result, it is standard practice in the aerospace industry to use Monte Carlo simulations to test the performance of a robust controller. This method essentially evaluates a large number of simulations with random dynamics, in order to provide statistical guarantees for the worst-case behaviour of the closed-loop system. However, while large iterations (approx. 1000) would be required for a hard proof, typical simulation numbers are much lower (around 300) due to computational costs, which can render the results of the analysis unreliable [10, 11].

4.1 Methodology

To expand the capabilities of the V&V process without resorting to a Monte Carlo campaign whose drawbacks have been detailed in the previous sections, a worst-case uncertainty construction method is used that was developed by Patartics et al. It maximizes the gain of a system at multiple user-defined frequencies and is currently applied in the analysis of flutter suppression in flexible aircraft [12, 24].

4.1.1 Modelling for Uncertainty

Considering the varied dynamics of reaction wheels, it was determined that their model should be adjusted with dynamic uncertainty. First, $\Delta(s)$ is created with Matlab's `ultidyn` function which generates a fourth-order LTI model with a gain bound of 1. Then, a filtering function $W_{UC}(s)$ is defined that produces a roughly 1 dB variance in the DC gain and a 5 dB/decade variance in the roll-off of the reaction wheel model.

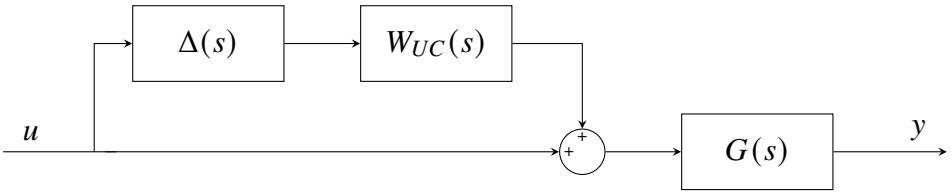

Fig. 7 Block diagram of dynamic uncertainty applied to some plant G(s)

Parametric uncertainty is also introduced to the mass and inertia of the system, as well as the flexible characteristics. This is in line with the recommendation made by several authors in V&V publications, and in this project, it is achieved by the uncertainty of the tank mass and panel rotation angle [10, 11]. The ranges for the damping ratio and frequency are in line with SZTAKI's usual assumptions, and the rotation angle was calculated based on the uncertainty in the exact rotation angle of the panel (table 1).

Table 1 Uncertain parameters for multifrequency worst-case uncertainty construction

Parameter	Value	Range
Tank mass multiplier	0.5	0-1
Panel rotation angle	0	-0.2 - 0.2 rad
Panel damping ratio multiplier	1	0.90-1.10
Panel frequency multiplier	1	0.98-1.02

4.1.2 Worst-Case Construction Algorithm

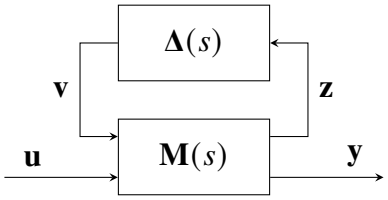

Fig. 8 Interconnection of an uncertain system for upper LFT

Consider the block diagram in figure 8, with the stable MIMO LTI system $\mathbf{M}(s)$ and its corresponding MIMO uncertainty block $\mathbf{\Delta}(s)$. There, $\mathbf{M}(s)$ is an augmented version of the nominal system model with widened output and input channels to tie the effect of uncertainty into the model. The exact description of how this uncertainty is acting in the system dynamics is described by $\mathbf{\Delta}(s)$, which has two components.

The first one is parametric uncertainty, which is the main type of uncertainty introduced to the system so far. It describes deviations in the value of certain physical parameters. The second one is dynamic uncertainty, which represents unmodelled behaviour in the system. Examples include high-frequency vibrations or residual dynamics from model reduction. The most important criterion is that uncertain dynamics must be stable and unit norm-bounded, but they can be weighted to adjust their magnitude. Partition the system model so that the upper left block has compatible dimensions with the uncertainty block,

$$\mathbf{M} = \begin{bmatrix} \mathbf{M}_{11} & \mathbf{M}_{12} \\ \mathbf{M}_{21} & \mathbf{M}_{22} \end{bmatrix}. \tag{7}$$

The upper LFT of $\mathbf{M}$ and $\mathbf{\Delta}$ is then defined as $\mathbf{F}_u(\mathbf{M}, \mathbf{\Delta}) = \mathbf{M}_{22} + \mathbf{M}_{21}\mathbf{\Delta}(\mathbf{I} - \mathbf{M}_{11}\mathbf{\Delta})^{-1}\mathbf{M}_{12}$, and the uncertain system is $\mathbf{P}(\mathbf{\Delta}, s) = \mathbf{F}_u(\mathbf{M}(s), \mathbf{\Delta}(s))$. Now, assume the following: $\mathbf{\Delta}(s) \in \mathbb{\Delta}$, $\mathbf{P}(\mathbf{\Delta}, s)$ is robustly stable (i.e. stable for $\forall \mathbf{\Delta}(s) \in \mathbb{\Delta}$), given are a set frequencies $[\omega_k]_{k=1}^{N_\omega}$ and worst-case gain lower bounds $[L_k]_{k=1}^{N_\omega}$. Then, define the function $J : \mathbb{\Delta} \to \mathbb{R}$ that it is the sum of gains at the given frequencies:

$$J(\mathbf{\Delta}(s)) = \sum_{k=1}^{N_\omega} \bar{\sigma}\left(\mathbf{F}_u(\mathbf{M}(j\omega_k), \mathbf{\Delta}(j\omega_k))\right). \tag{8}$$

The worst-case uncertainty sample construction problem is to find $\mathbf{\Delta}_m(s) \in \mathbb{\Delta}$ for which $J(\mathbf{\Delta}_m(s))$ is maximized. The function J has a theoretical upper bound, which is the sum of the worst-case gain lower bounds at the given frequencies: $J_U = \sum_{k=1}^{N_\omega} L_k$. It is clear, that $J(\mathbf{\Delta}(s)) \leq J_U$, $\forall \mathbf{\Delta}(s) \in \mathbb{\Delta}$. If the system is only subjected to dynamic uncertainty, then it is possible to find a $\mathbf{\Delta}_m(s)$ that $J(\mathbf{\Delta}_m(s)) = J_U$, based on the boundary Nevanlinna-Pick interpolation [25]. However, in the case of mixed uncertainty with both dynamic and parametric components, it is generally not possible to find such a $\mathbf{\Delta}_m(s)$, because parametric uncertainty couples the frequencies together and different values of the same parameter may be required to achieve the lower bound at each frequency.
The worst-case uncertainty construction method applied in this section addresses these issues by using a nonlinear optimization method that performs an efficient search of the full range of parametric uncertainty as well as a boundary Nevanlinna-Pick interpolation of dynamic uncertainty [12, 24].

4.2 Performance of the Closed Loop

Analyzing the performance of a closed-loop control system with the worst-case uncertainty construction method is an iterative process which offers increased speed and reliability compared to random sampling-based Monte Carlo methods. First, an uncertain model is constructed with both parameter and dynamic uncertainty. Then, the uncertain transfer function of the cascade loop from the 3 reference angles to the 6 pointing angles is converted to an LFT model that is passed to the optimization script along with two parameter sets: the relevant frequencies and the input-output pair where the effect of uncertainty should be maximized. The selected channel can either correspond to reference tracking or disturbance rejection.

The result is an exact parametrization of the uncertain block, which is used to update the high-fidelity nonlinear simulation environment and evaluate pointing performance. To speed up the process, the most interesting frequencies are selected iteratively by first checking the step-tracking characteristics of the adjusted closed-loop and shifting the set of frequencies as needed. Usually, most pessimistic models are reached when the frequencies are placed in the peaks and inflection points of the Bode magnitude plot.

The H_∞ loop has proven itself to be robust enough against uncertainty in the multi-frequency analysis. Using the method, the magnitude of disturbances on the roll and pitch outputs increased by 35 dB and 20 dB, respectively, which translates to a major time-domain rise in the oscillations in all axes. Step

tracking is slightly affected in the form of some lightly dampened oscillations in the roll and pitch loops. It is clearly visible on the plots that the worst cases found by the method (in red) produce far worse performance than random samples (in grey), further motivating the use of the algorithm. One exception would be the disturbance rejection of the yaw loop, which was optimized for settling time instead of overshoot. This was a deliberate choice, as long-term errors have a larger impact on dynamics compared to transients.

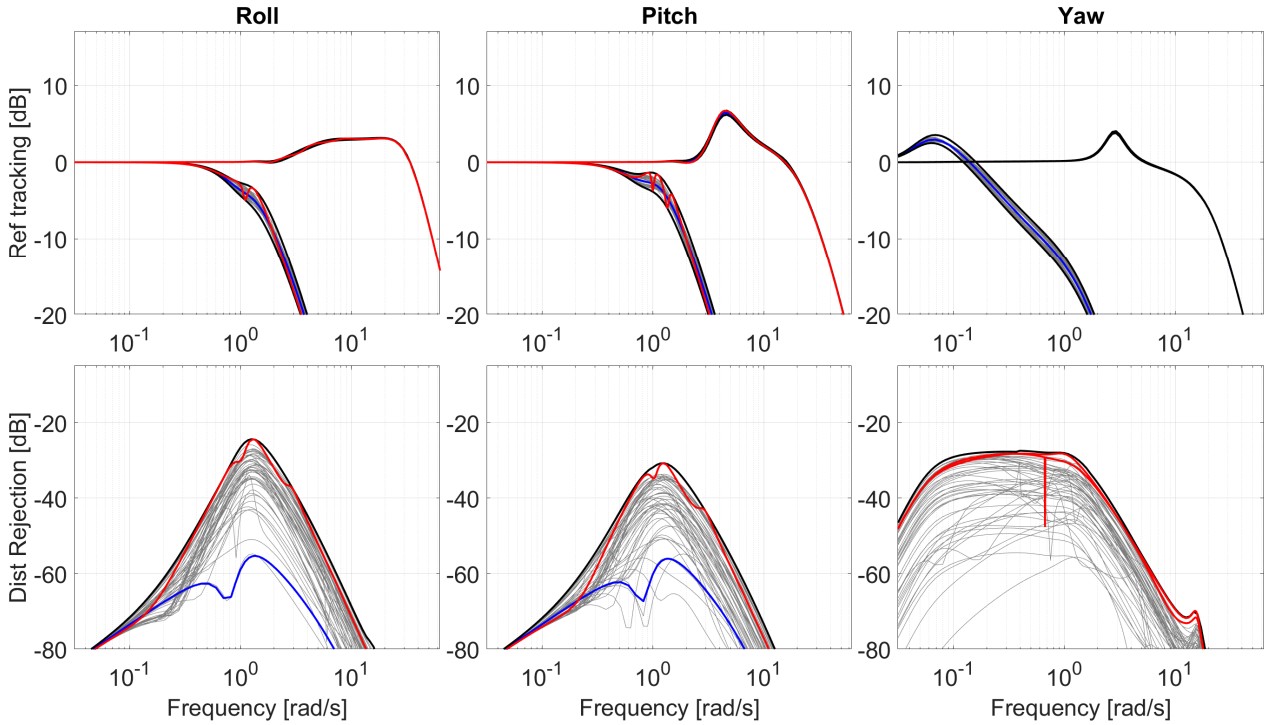

Fig. 9 Bode magnitude plots of the cascade loop in nominal (blue), worst (red), and random cases (grey)

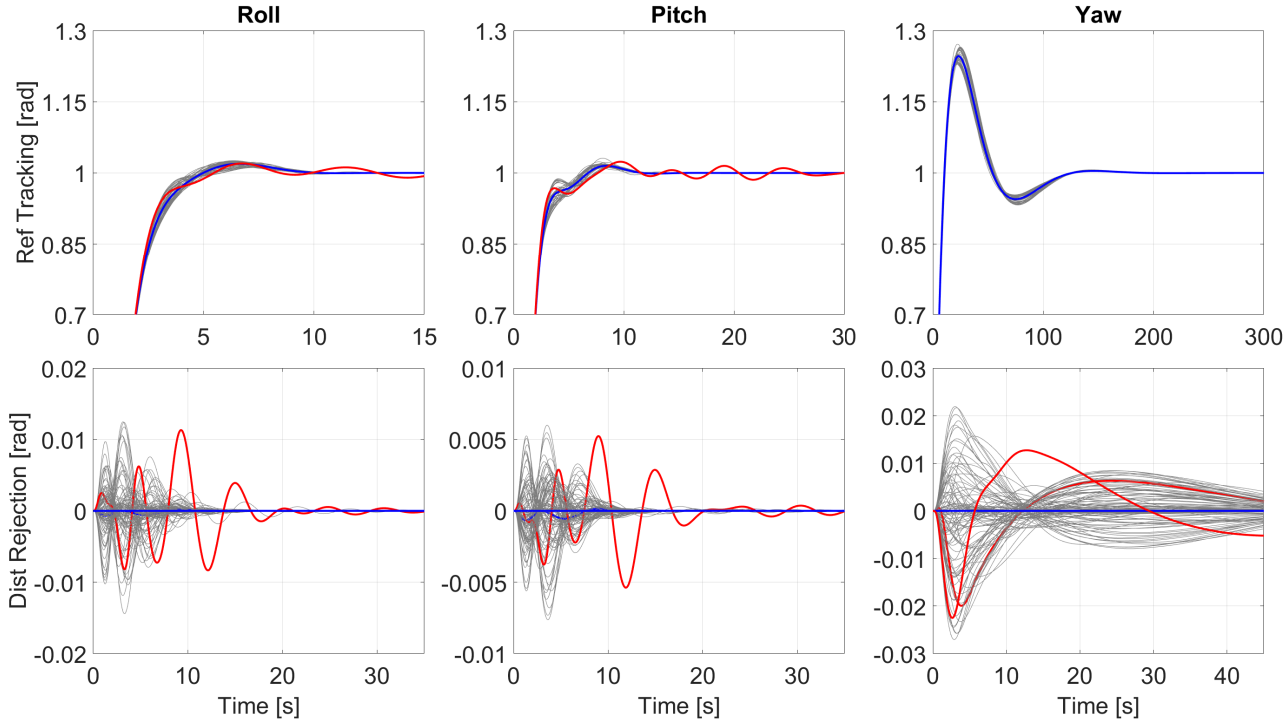

Fig. 10 Step response of the H_∞ outer loop in the nominal (blue), worst (red), and random cases (grey)

Three pointing performance indicators are assessed in the nonlinear environment, according to the ECSS. Absolute performance error (APE) is the first and simplest one, and it is generally used in the control design of all pointing systems. It is the absolute difference of the current line-of-sight vector from the desired one in terms of pointing angles. Using a 10 sec measurement window, the mean performance error (MPE) and relative performance error (RPE) can be defined, with MPE being equivalent to the windowed-time error signal, and RPE arising as the difference between APE and MPE [26]. Using a scenario to track two points in South Holland with a 15-second transient stage between the precise segments, both loops have very low susceptibility to uncertainty, highlighting the importance of robust control. For the control loop, the most significant effect is perhaps a 29% increase in APE and 10% in RPE for roll reference tracking, and the effect of uncertainty seems to be diminishing with time as the controller brings system dynamics close to nominal for all cases, even with large initial errors.

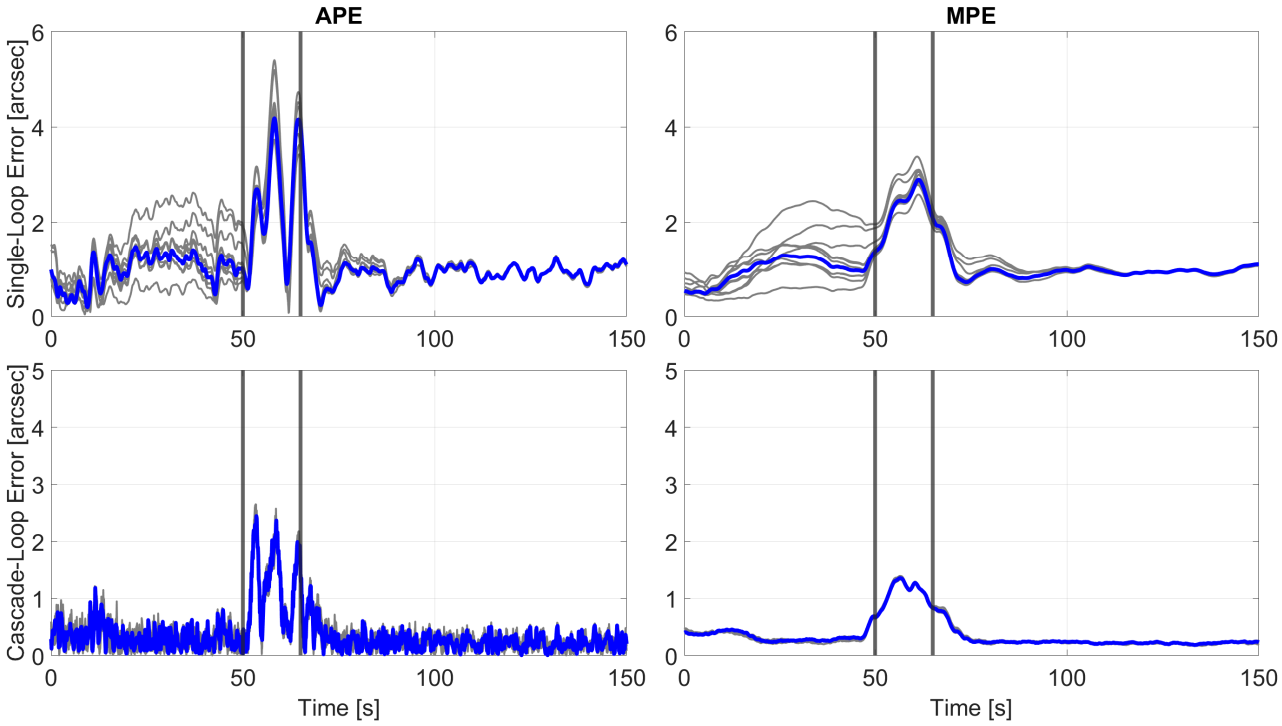

Fig. 11 Simulation results for worst cases (grey) and nominal case (blue) with the cascade H_∞ loop

Table 2 Worst-case pointing indices of output channels for Roll tracking in the outer and inner H_∞ loops

Worst cases	APE_{avg} [%]	MPE_{min} [%]	MPE_{max} [%]	RPE_{avg} [%]
ϕ	29.1943	-6.749	77.511	10.5943
ϕ_i	-5.4575	-2.6953	-6.3912	-0.3264
θ	6.1577	-2.3725	9.8517	-0.5488
θ_i	8.315	-5.8852	15.7487	-0.7847
ψ	-17.2412	-30.6985	-5.6572	-10.1902
ϕ	-4.0103	-0.7906	2.9481	-5.4492
ϕ_i	4.5953	2.1361	0.1395	5.2307
θ	-2.8671	-4.93	-0.6716	-7.1753
θ_i	-1.1565	-7.8672	0.6591	-2.6894
ψ	-1.7688	-4.0452	2.3889	-2.4326

Table 3 Worst-case pointing indices of output channels for Pitch tracking in the outer and inner H_∞ loops

Worst cases	APE_{avg} [%]	MPE_{min} [%]	MPE_{max} [%]	RPE_{avg} [%]
ϕ	7.3854	12.127	11.7233	0.6467
ϕ_i	6.3038	3.2714	10.4044	0.8901
θ	-1.2012	39.8143	-1.6015	3.2027
θ_i	-6.0763	-7.4852	-3.5371	-2.8062
ψ	17.7994	2.0899	40.7737	1.7107
ϕ	-2.978	-0.8368	-3.6655	-5.6737
ϕ_i	1.5117	1.1538	0.5031	1.9138
θ	-5.046	-0.111	-5.2367	-4.6331
θ_i	1.2504	1.2171	1.1474	2.5651
ψ	-2.792	-7.1414	0.8685	-4.3276

5 Conclusion

The main research objective of the project is to find a way to improve the pointing precision of flexible spacecraft. When looking at reference tracking characteristics in the high-fidelity simulator, the outer loop achieved roughly 1 arcsec error with a cutoff frequency of 1 rad/s, and it was determined that even for the worst-case mixed uncertainty cases the robust controller can converge to this error level. The inner loop showed no increase in pointing error when exposed to uncertainty, keeping a steady 0.4 arcsec windowed-time error with a cutoff frequency of 20 rad/s. As a result, the control design process is deemed successful, and the developed V&V framework was able to significantly increase the reliability of the designs.

A drawback of the current model is the relative difficulty in calculating accurate reaction forces, stemming from the complex nonlinear dynamics of the system and the numerical conditioning problem of small-scale isolator movements and large-scale orbital perturbations on the spacecraft. While it has been determined that the current mass of the isolator platform is not large enough to cause significant disturbances to the cascade control loop, there is an ongoing effort to remedy this issue through the creation of a combined mechanical model of the entire spacecraft. This way, the orbital dynamics of the spacecraft CoG can be decoupled from the internal mechanics of the system, allowing for more precise simulations and lower susceptibility to numerical errors.

Another further goal is the exploration of other methods in robust control. One way forward would be mixed-sensitivity loop shaping, which promises a better way to specify performance and robustness for various frequency ranges. Currently, this would be done by including Pittelkau functions in not just the validation, but also the design process, which increases the required manual tuning effort exponentially. Another approach would be to combine the design process and the reduction of the inner and outer loops into a single step, using structured H_∞-based design. This promises to improve the numerical conditioning and cross-operability of the system, leading to an easier implementation for real hardware.

In essence, the answer to the main research question can be explained in three parts. First, even if the structural dynamics and onboard microvibration sources are weak, single-loop control design has to take the flexible modes into account because system performance is greatly limited by the bandwidth and saturation limits of actuators. A cascade control loop with a vibration-isolated payload solves this issue by expanding the frequency range of the controller and offloading control requirements from the main loop to the isolator, leading to more relaxed control in the outer loop and higher pointing performance in the inner loop. Second, purely frequency-domain validation processes are not sufficient to prove robustness, as time-domain performance is vastly more important considering the standard precise pointing indices.

Nonlinear high-fidelity modelling techniques offer significant improvements in the validation of control design by the reliable evaluation of system behaviour in identified worst cases. Third, there are plenty of articles focusing separately on high-fidelity modelling, advanced control, or verification&validation techniques, but individually these fields contain significant blind spots. Only their synergistic combination can provide a robust framework for the control engineering of flexible space structures.

Acknowledgments

The research reported in this paper is part of project no. SZTAKI-NVA-01, implemented with the support provided by the Ministry of Innovation and Technology of Hungary from the National Research, Development and Innovation Fund, financed under the TKP2021 funding scheme.

References

[1] Valentin Preda. *Robust microvibration control and worst-case analysis for high pointing stability space missions*. PhD thesis, Université de Bordeaux, 2017.

[2] Paolo Gasbarri, Riccardo Monti, Giovanni Campolo, and Chiara Toglia. Control-oriented modelization of a satellite with large flexible appendages and use of worst-case analysis to verify robustness to model uncertainties of attitude control. *Acta Astronautica*, 81(1):214–226, 2012.

[3] Cornelius J Dennehy. A survey of reaction wheel disturbance modeling approaches for spacecraft line-of-sight jitter performance analysis. In *Proc. European Space Mechanisms and Tribology Symp. Munich, Germany*, 2019.

[4] Bing Xiao, Qinglei Hu, and Youmin Zhang. Adaptive sliding mode fault tolerant attitude tracking control for flexible spacecraft under actuator saturation. *IEEE Transactions on Control Systems Technology*, 20(6):1605–1612, 2011.

[5] T Loquen, H De Plinval, C Cumer, and D Alazard. Attitude control of satellites with flexible appendages: a structured h_∞ control design. In *AIAA Guidance, Navigation, and Control Conference*, page 4845, 2012.

[6] Hyochoong Bang and Choong-Seok Oh. Predictive control for the attitude maneuver of a flexible spacecraft. *Aerospace science and technology*, 8(5):443–452, 2004.

[7] Takanori Iwata, Haruyuki Ishida, and Yuji Osawa. Advanced land observing satellite (alos): enabling technologies and platform performance. In *Sensors, Systems, and Next-Generation Satellites XII*, volume 7106, pages 113–125. SPIE, 2008.

[8] Valentin Preda, Jérôme Cieslak, David Henry, Samir Bennani, and Alexandre Falcoz. Robust microvibration mitigation and pointing performance analysis for high stability spacecraft. *International Journal of Robust and Nonlinear Control*, 28(18):5688–5716, 2018.

[9] John E McInroy, John F O'Brien, and Gregory W Neat. Precise, fault-tolerant pointing using a stewart platform. *IEEE/ASME transactions on mechatronics*, 4(1):91–95, 1999.

[10] Wenfei Wang, Prathyush Menon, Declan Bates, and Samir Bennani. Verification and validation of attitude and orbit control systems for flexible satellites. In *AIAA Guidance, Navigation, and Control Conference*, page 5953, 2009.

[11] W Wang, PP Menon, DG Bates, and S Bennani. Robustness analysis of attitude and orbit control systems for flexible satellites. *IET control theory & applications*, 4(12):2958–2970, 2010.

[12] Bálint Patartics, Peter Seiler, Béla Takarics, and Bálint Vanek. Worst case uncertainty construction via multifrequency gain maximization with application to flutter control. *IEEE Transactions on Control Systems Technology*, 31(1):155–165, 2022.

[13] János Bezsilla, Béla Takarics, Bálint Vanek, and Jian Guo. Parameter uncertainty analysis in precise pointing control of flexible spacecraft. *IFAC-PapersOnLine*, 55(20):241–246, 2022.

[14] Jawhar Chebbi, Vincent Dubanchet, José Alvaro Perez Gonzalez, and Daniel Alazard. Linear dynamics of flexible multibody systems. *Multibody System Dynamics*, 41(1):75–100, 2017.

[15] Daniel Alazard and Francesco Sanfedino. Satellite dynamics toolbox for preliminary design phase. In *43rd Annual AAS Guidance and Control Conference*, volume 30, pages 1461–1472, 2020.

[16] Francesco Sanfedino. *Experimental validation of a high accuracy pointing system*. PhD thesis, Toulouse, ISAE, 2019.

[17] Francesco Sanfedino, Daniel Alazard, Valérie Pommier-Budinger, Alexandre Falcoz, and Fabrice Boquet. Finite element based n-port model for preliminary design of multibody systems. *Journal of Sound and Vibration*, 415:128–146, 2018.

[18] Dae-Kwan Kim. Micro-vibration model and parameter estimation method of a reaction wheel assembly. *Journal of Sound and Vibration*, 333(18):4214–4231, 2014.

[19] Rebecca A Masterson, David W Miller, and Robert L Grogan. Development and validation of reaction wheel disturbance models: empirical model. *Journal of sound and vibration*, 249(3):575–598, 2002.

[20] Sigurd Skogestad and Ian Postlethwaite. *Multivariable feedback control: analysis and design*. john Wiley & sons, 2005.

[21] Andre Preumont. *Vibration control of active structures*, volume 2. Springer, 1997.

[22] A Abu Hanieh. *Active isolation and damping of vibrations via Stewart platform*. PhD thesis, PhD Thesis, Université Libre de Bruxelles, Active Structures Laboratory, 2003.

[23] Ricardo Rodrigues, Valentin Preda, Francesco Sanfedino, and Daniel Alazard. Modeling, robust control synthesis and worst-case analysis for an on-orbit servicing mission with large flexible spacecraft. *Aerospace Science and Technology*, page 107865, 2022.

[24] Bálint Patartics. Uncertain systems: analysis and synthesis with application to flutter suppression control. *PhD Thesis*, 2022.

[25] Joseph Ball, Israel Gohberg, et al. *Interpolation of rational matrix functions*, volume 45. Birkhäuser, 2013.

[26] T Ott, W Fichter, S Bennani, and S Winkler. Precision pointing hinf control design for absolute, window-, and stability-time errors. *CEAS Space Journal*, 4:13–30, 2013.